

A statistical jet-noise model based on the resolvent framework

Aaron Towne*, Guillaume A. Brès†, Sanjiva K. Lele‡

This paper continues the development of a recently proposed resolvent-based model designed to capture the full second-order statistics of turbulent jets, which are required to obtain accurate noise estimates. The model requires an approximation of the cross-spectral density tensor of certain nonlinear forcing terms, and the focus of this paper is to characterize the properties of these statistics in a high-Reynolds-number subsonic jet. We show that the power spectral density of the forcing is independent of frequency over a range of almost two orders-of-magnitude. The coherence of the forcing consists of peaks that are spatially compact compared to the coherence length-scales of the flow variables. The widths of these peaks depend on spatial location but not frequency, while the streamwise and radial wavelenghts of the coherence depend on frequency but not spatial location. We propose a simple fit function in frequency space that captures these properties and show that it leads to good approximations of the LES forcing statistics. Some of the parameters in the model are well-approximated by quantities that could be obtained from a Reynolds-averaged Navier-Stokes simulation. Finally, we show that the properties of the forcing statistics are completely different for a low-Reynolds-number jet, which may be indicative of direct nonlinear interactions amongst wavepackets which are absent in the high-Reynolds-number jet.

I. Introduction

Numerous studies have identified large-scale coherent wavepacket structures within turbulent jets as an important source of noise.¹ The typical approach to modeling wavepackets is to approximate them as linear modal solutions of the Navier-Stokes equations linearized about the long-time mean of the turbulent flow-field. The near-field wavepackets obtained from these linear models show compelling agreement with those deduced from experimental and simulation data,²⁻⁴ but the associated far-field acoustic radiation is under-predicted by as much as 40 dB in subsonic jets.^{5,6}

A hypothesized explanation for this discrepancy is acoustic amplification due to wave-packet intermittency or “jitter”.⁷ Unlike the wavepackets obtained from linear models, real wavepackets in turbulent jets undergo intermittent, low frequency modulation of their envelope and phase. The acoustic efficiency of a wavepacket is highly sensitive to these modulations, so flow events that lead to small near-field changes in the wavepacket can give rise to large amplifications in the acoustic field. This suggests that the average wavepacket does not produce the average sound in subsonic jets, a conclusion also reached via statistical analysis of simulation data from both low Reynolds number and high Reynolds number subsonic jets.^{8,9} Instead, wavepacket jitter and the resulting noise amplification is described by two-point, second-order statistics of the flow, which are not properly captured by linear models.¹⁰

This paper continues the development of the model recently formulated by Towne *et al.*¹¹ aimed at capturing the full second-order statistics of the jet. The so-called resolvent operator¹² arises naturally in this development, so the model can be understood as a modified form or statistical interpretation of resolvent analysis,^{13,14} which has been applied to jets by several authors.¹⁵⁻¹⁷ In particular, the resolvent operator relates the second-order statistics of the flow variables and the second-order statistics of the nonlinear terms that are neglected by purely linear models.

*Postdoctoral Fellow, Center for Turbulence Research, Stanford University

†Senior Research Scientist, CASCADE Technologies

‡Professor, Aeronautics and Astronautics and Mechanical Engineering, Stanford University

The main contribution of this paper is an analysis and characterization of the statistics of the nonlinear forcing terms in both high and low Reynolds number jets. The forcing statistics are investigated using large-eddy-simulation data, and the goal is to chronicle their properties and gain insight into how they should be approximated within the statistical model. To this end, we compare the properties of the LES statistics with a common fit-function used to represent similar source terms in other statistical jet noise models and suggest a modified form that better captures the trends in the data. Finally, we give some preliminary suggestions on how the free parameters in the fit function might be eliminated using quantities that could be obtained from a Reynolds-averaged Navier-Stokes (RANS) simulation.

The remainder of the paper is organized as follows. The statistical resolvent-based model is reviewed and compared to other statistical models in Section II. The LES data that is used throughout the paper is described in Section III. The forcing statistics of the high-Reynolds-number jet are investigated in Section IV and fitting function for this data are discussed in Section V. The low-Reynolds-number jet is considered in Section VI and the main results of the paper are summarized in Section VII.

II. A resolvent-based statistical jet-noise model

We begin by reviewing the statistical resolvent-based model formulated by Towne *et al.*¹¹ The basic idea is to derive an expression for the cross-spectral density of the flow-field, which describes wavepacket jitter and is necessary to predict far-field noise.¹⁰ This leads to a relationship in terms of the resolvent operator between the second-order statistics of the flow-field and nonlinear terms that are neglected in liner models. While in one sense this simply replaces the need to model the flow statistics with the need to model the forcing statistics, we will see that the form of the latter make them substantially more amenable to modeling.

II.A. Resolvent analysis

The starting point of the model is the full compressible Navier-Stokes equations, which can be written conceptually as

$$\frac{\partial q}{\partial t} = \mathcal{F}(q), \quad (1)$$

where q is a state-vector of flow variables. Substituting the standard Reynolds decomposition

$$q(x, r, \theta, t) = \bar{q}(x, r) + q'(x, r, \theta, t) \quad (2)$$

into equation (1) and isolating the terms that are linear in q' yields an equation of the form

$$\frac{\partial q'}{\partial t} - \mathcal{A}(\bar{q}) q' = f(\bar{q}, q'), \quad (3)$$

where

$$\mathcal{A}(\bar{q}) = \frac{\partial \mathcal{F}}{\partial q}(\bar{q}) \quad (4)$$

and f contains the remaining nonlinear terms. It is usually the case that only a limited portion of the state q' is of interest. This can be formalized by defining an output quantity,

$$y = \mathcal{C}q', \quad (5)$$

consisting of any linear combination of the state. For example, y could represent the far-field acoustic pressure.

Since the jet is round and statistically stationary, it is valid to apply Fourier transforms in the azimuthal direction and time to equations (3) and (5), giving

$$(i\omega I - \mathcal{A}_m) \hat{q} = \hat{f}, \quad (6)$$

$$\hat{y} = \mathcal{C}\hat{q}, \quad (7)$$

where ω is the angular frequency, m is the azimuthal wavenumber, and \mathcal{A}_m is the operator \mathcal{A} with $\frac{\partial}{\partial \theta}$ replaced by im . The transformed variables \hat{q} , \hat{y} , \hat{f} are functions of (x, r, m, ω) . The input/output relation

between the nonlinear (input) term \hat{f} and the output \hat{y} is obtained by eliminating \hat{q} from equations (6-7), giving

$$\hat{y} = \mathcal{R}\hat{f} \quad (8)$$

with

$$\mathcal{R} = \mathcal{C}(i\omega I - \mathcal{A}_m)^{-1}. \quad (9)$$

Note that $(i\omega I - \mathcal{A}_m)$ is always invertible if \mathcal{A} is stable, i.e., the real part of all of its eigenvalues is negative.

Resolvent modes are given by the singular value decomposition of the resolvent operator,

$$\mathcal{R} = U\Sigma V^*. \quad (10)$$

The singular values, which appear within the diagonal positive-semi-definite matrix Σ , give the square root of the optimal gains between the input and output modes defined by the right and left singular vectors contained in the columns of the orthonormal matrices V and U , respectively. The asterisk indicates a conjugate transpose.

II.B. Statistics in terms of the resolvent operator

The second-order statistics of the input and output are obtained by averaging over an ensemble of solutions of equation (1) that have undergone different random external excitation. Specifically, we define the cross-spectral-density (CSD) matrices $S_{\hat{y}\hat{y}} = \langle \hat{y}\hat{y}^* \rangle$ and $S_{\hat{f}\hat{f}} = \langle \hat{f}\hat{f}^* \rangle$, where $\langle \cdot \rangle$ is the expectation operator. Using equation (8), these two CSD matrices are related as

$$S_{\hat{y}\hat{y}} = \langle \hat{y}\hat{y}^* \rangle = \langle \mathcal{R}\hat{f}\hat{f}^*\mathcal{R}^* \rangle = \mathcal{R}\langle \hat{f}\hat{f}^* \rangle\mathcal{R}^* = \mathcal{R}S_{\hat{f}\hat{f}}\mathcal{R}^*. \quad (11)$$

Equation (11) provides an exact relationship between the second-order statistics of the nonlinear term \hat{f} and the output \hat{y} in terms of the resolvent operator \mathcal{R} .

The simplest approximation of the forcing is to treat it as being completely uncorrelated in space and time with equal amplitude everywhere in space, i.e., unit-amplitude white-noise. Then $S_{\hat{f}\hat{f}} = I$ and inserting this into equation (11) shows that the CSD of the output is completely defined by the resolvent operator:

$$S_{\hat{y}\hat{y}} = \mathcal{R}\mathcal{R}^* = U\Sigma V^*V\Sigma U^* = U\Sigma^2 U^*. \quad (12)$$

Since U is orthonormal, the last expression in equation (12) shows that the resolvent output modes are the principal components of the output CSD matrix, i.e., the spectral-proper-orthogonal-decomposition (SPOD) modes of the flow, if the forcing is unit-amplitude white-noise. This result has been recently reported by several authors.^{9, 11, 17, 18}

Equation (11) also provides the foundation for defining a modified resolvent operator that accounts for correlated nonlinear forcing, which is key for properly capturing the second-order flow statistics needed to correctly model the noise. To do so, we begin with a factorization of the forcing CSD of the form

$$S_{\hat{f}\hat{f}} = FF^*, \quad (13)$$

which can represent a Cholesky decomposition or an SPOD eigenvalue decomposition $S_{\hat{f}\hat{f}} = V_F\Sigma_F^2 V_F^*$ with $F = V_F\Sigma_F$. Next, define a modified resolvent operator

$$\tilde{\mathcal{R}} = \mathcal{R}F \quad (14)$$

and its singular value decomposition

$$\tilde{\mathcal{R}} = \tilde{U}\tilde{\Sigma}\tilde{V}^*. \quad (15)$$

Unless F is orthonormal (which is the case when the forcing is white), the singular values and vectors of \mathcal{R} and $\tilde{\mathcal{R}}$ are not the same; including the correlated forcing fundamentally alters the modes. Equation (11) can be written in terms of the modified resolvent operator as

$$S_{\hat{y}\hat{y}} = \tilde{\mathcal{R}}\tilde{\mathcal{R}}^* = \tilde{U}\tilde{\Sigma}\tilde{V}^*\tilde{V}\tilde{\Sigma}\tilde{U}^* = \tilde{U}\tilde{\Sigma}^2\tilde{U}^*. \quad (16)$$

Therefore, the output modes of the modified resolvent operator are the SPOD modes of \hat{y} . Furthermore, the gains give the energy in each mode. As a result, the modified resolvent modes provide an optimal representation of the output and properly represent the full second-order flow statistics of the jet.

Alternatively, we can write the output CSD in terms of standard resolvent output modes weighted by expansion coefficients that depend on the forcing statistics:

$$S_{\hat{y}\hat{y}} = UE^2U^* \quad (17)$$

with $E^2 = \Sigma V^* S_{\hat{f}\hat{f}} V \Sigma$. Comparing this expression with equation (12), we see that E^2 has taken the place of Σ^2 ; the non-white forcing has changed the contribution of each resolvent mode to the output statistics. The remaining task in obtaining a predictive model is to construct an appropriate approximation of the forcing CSD matrix $S_{\hat{f}\hat{f}}$.

II.C. Comparison with other jet noise models

The idea of approximating the forcing statistics makes our approach similar to two other types of jet-noise models that exist in the literature. The closest connection is with a collection of stochastic models in which time-dependent forcing terms for the linearized Navier-Stokes equations are synthesized in the time domain such that they obey prescribed statistics on average. For example, Bechara *et al.*¹⁹ introduced the stochastic noise generation and radiation model, in which the forcing is defined by a random time-dependent velocity field whose statistical properties mimic homogeneous isotropic turbulence. The model was modified by Billson *et al.*²⁰ and Lafitte *et al.*²¹ to account for anisotropy and turbulent sweeping effects, respectively. Siefert & Ewert²² developed a similar approach in which stochastic velocities with prescribed statistics are generated using the random particle-mesh method and used to realize the source terms suggested by Tam & Auriault.²³ One advantage of our resolvent-based approach over these time-domain stochastic methods is that our model acts directly on *statistics* of the forcing terms and therefore avoids the need to run long time-domain simulations to converge the noise statistics (even with long simulations the statistics remain noticeably noisy in most applications of these stochastic approaches).

Second, our model has some similarities with Goldstein’s²⁴ generalized acoustic analogy, in which the linearized Navier-Stokes equations are used to derive a Green’s function relating source terms consisting of two-point, two-time fourth-order correlations of the near-field jet with far-field acoustic radiation. Although very specific variables are used for the acoustic analogy, these correlations are conceptually similar to the forcing cross-spectral densities in our approach, and in particular are analogous (but not identical) to the inverse Fourier transform of the forcing CSD. However, we will see in Section V that modeling the forcing statistics in the frequency domain rather than the time domain allows for a more faithful representation of the key properties of the forcing within the frequency range of interest.

The modal decomposition of the resolvent operator provides several additional benefits to our approach compared to either of the other two methods. First, each resolvent mode provides an unambiguous link between some portion of the forcing field, the near-field flow structures excited by that forcing, and the far-field noise emitted by those structures. This is extremely useful for interpreting and isolating the physical noise production mechanisms. Second, the resolvent modes provide a compact description of the linear noise production and propagation mechanisms that can be used as a basis for further model reduction.

III. LES databases and spectral estimation

We use data from two different high-fidelity large-eddy simulations of isothermal Mach 0.9 jets issued from the same convergent-straight nozzle. The simulations were performed with the compressible flow solver “CharLES” developed at Cascade Technologies.²⁵ The first jet has a Reynolds number (based on the nozzle diameter) of one million. The boundary layer is fully turbulent at the nozzle exit and the accuracy of the LES data was verified via extensive comparison with experimental measurements. More information on the LES of this jet and its validation are available in previous publications.^{26,27} The second jet has a Reynolds number of 3600, chosen to match the value from a previous DNS simulation.²⁸ This jet is initially laminar and contains organized vortices in the shear-layer that eventually break down and lead to transition well downstream.

The nonlinear forcing terms for both jets are computed using the LES code. This ensures consistency with the LES approximation of the Navier-Stokes equations and minimizes numerical contamination compared to alternative methods. Additional details can be found in the thesis of the first author.¹⁸

Spectra are estimated using Welch’s method. The flow and forcing time series are partitioned into an ensemble of overlapping blocks, windowed, and transformed in time and azimuth using discrete Fourier

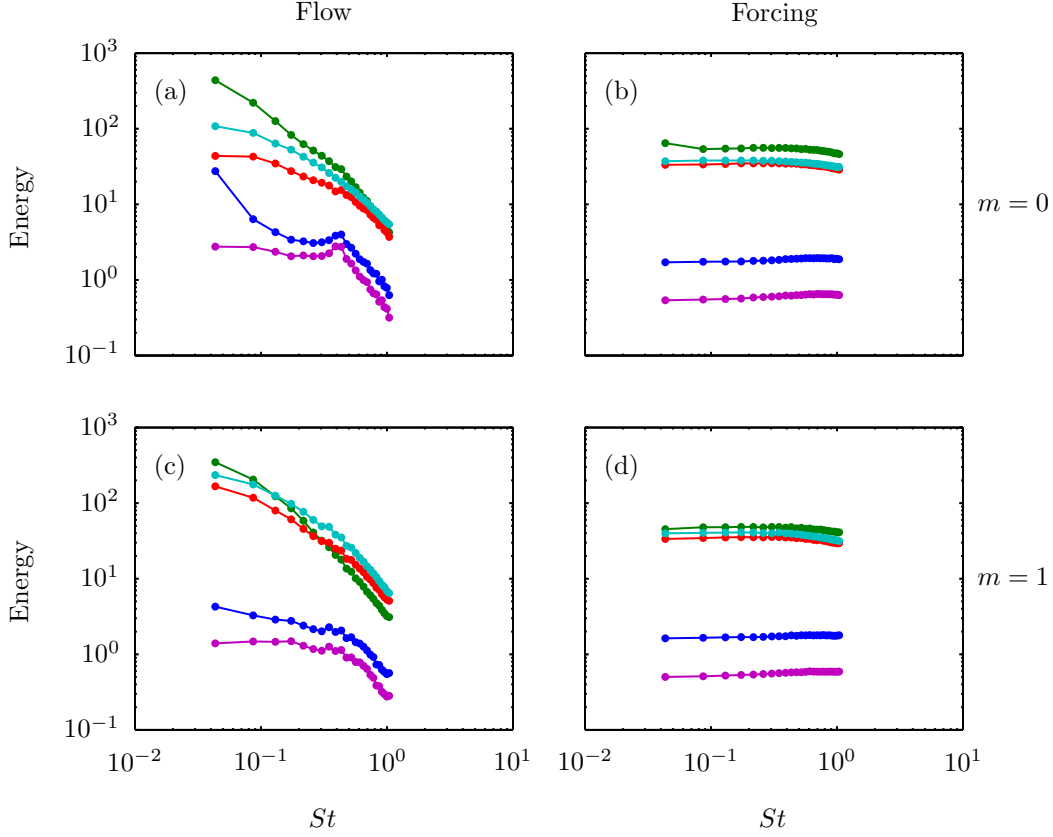


Figure 1: Total energy, defined as the spatially-integrated power spectral density, for each flow (left) and forcing (right) variable in the high-Reynolds-number jet as a function of frequency for the azimuthal modes $m = 0$ (top) and $m = 1$ (bottom). The flow variables are, from top to bottom, streamwise, radial, and azimuthal velocity, specific density, and pressure. The forcing terms act on the axial, radial, and azimuthal momentum equations, the continuity equation, and the energy equation.

transforms. We use blocks containing 256 instantaneous snapshots (covering about 50 acoustic time units) with 90% overlap and a standard Hann window. We have verified that our conclusions are not sensitive to these choices. The cross-spectra of the resulting Fourier modes are then ensemble-averaged to obtain the CSD matrix for each frequency, azimuthal wavenumber pair. Precisely,

$$S_{\hat{u}\hat{v}}(\vec{x}_i, \vec{x}_j, m, \omega) = \frac{1}{N} \sum_{k=1}^N \hat{u}^{(k)}(\vec{x}_i, m, \omega) (\hat{v}^{(k)}(\vec{x}_j, m, \omega))^*, \quad (18)$$

where $N = 356$ is the number of blocks, $\vec{x} = (x, r)$, and $\hat{u}^{(k)}$ and $\hat{v}^{(k)}$ are the Fourier modes of any two components of the input or output in the k -th block.

IV. Statistics of the nonlinear forcing terms in a high-Reynolds-number jet

In this section, we use the LES data for the jet with Reynolds number one million to characterize the properties of the CSD matrix $S_{\hat{f}\hat{f}}$ and suggest a fit-function that captures the key trends.

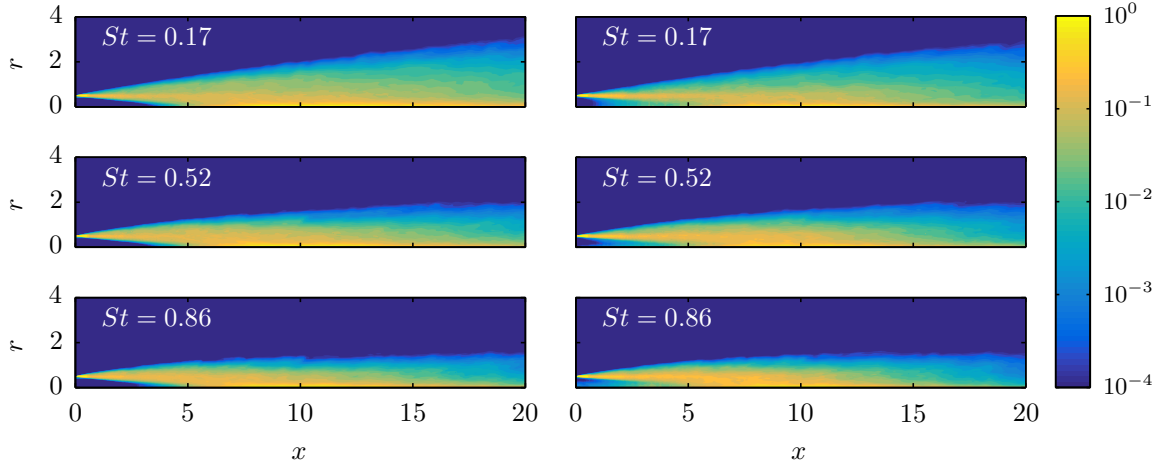


Figure 2: Power-spectral-densities of the streamwise-momentum forcing (left column) and energy forcing (right column) at $St = 0.17, 0.52,$ and 0.86 and $m = 0$.

IV.A. Power spectral densities

We begin by focusing on the power-spectral-densities (PSDs) $S_{\hat{a}\hat{a}}(\vec{x}_i, \vec{x}_i, m, \omega)$, which make up the diagonal entries in the CSD matrices. Figure 1 compares the total energy in each component of the forcing (associated with the mass, momentum, and energy equations) and in each flow variable (cylindrical velocities, pressure, and specific volume) for comparison. The total energy is defined here as the PSD integrated over the spatial domain, and results are shown as a function of frequency for the axisymmetric ($m = 0$) and helical ($m = 1$) azimuthal modes. Frequencies are reported in terms of the Strouhal number $St = fD/U_j$, where D is the nozzle-exit diameter, U_j is the jet velocity at the nozzle exit, and $f = \omega/2\pi$. The energy in the flow variables is highest at low frequencies and decays (almost) monotonically with increasing frequency, except for peaks in the pressure and specific volume at $St \approx 0.4$ that are related to trapped acoustic waves in the jet potential core.^{4,29–31} In contrast, the total energy in each forcing component is virtually independent of frequency in the range considered ($0.04 < St < 1.04$). The three momentum forcing terms have similar amplitudes, whereas the mass and energy forcing terms are nearly two orders-of-magnitude less energetic.

The spatial distribution of the PSD is also mostly independent of frequency. As an example, the PSDs of the axisymmetric portion of the streamwise-momentum and energy forcing terms are shown in Figure 2 for three frequencies. These results are characteristic of those observed for all five components of the nonlinear forcing term and all frequencies in the range $0.04 < St < 1.04$ for $m = 0$ and 1. The contour levels are logarithmically spaced and span four orders-of-magnitude (smaller values are saturated at the minimum level). No frequency-dependent scaling has been applied, but a single fixed (frequency-independent) parameter was used to scale the magnitude of the energy-equation forcing terms to the same level as the streamwise-momentum forcing terms (see Figure 1(b)). At all three frequencies, all components of the forcing PSD have a clear and consistent spatial structure. The forcing is essentially confined within the slowly-spreading shear-layer up to the end of the potential core and within the turbulent near-field of the fully-developed jet farther downstream. The magnitude of the forcing away from the jet and within the potential core is nearly zero. The only differences observed between the different frequencies occur well downstream along the outer fringes of the jet, a region that is not expected to be important for sound generation.

The remarkable degree of frequency independence observed in both the total energy and spatial structure of the PSD indicate that the amplitude of the forcing is white-in-time within the range $0.04 < St < 1.04$ for $m = 0$ and 1. In contrast, both the total energy and spatial structure of each flow variable are strongly dependent on frequency. This contrast suggests that the frequency-selection mechanisms responsible for the amplification of energy at low frequencies are embedded within the linearized Navier-Stokes operator rather than the nonlinear forcing terms. This is consistent with the recent observation by Schmidt *et al.*³² that gains of the leading resolvent modes scale like St^{-2} , which is similar to the scaling of the flow energy observed in Figure 1.

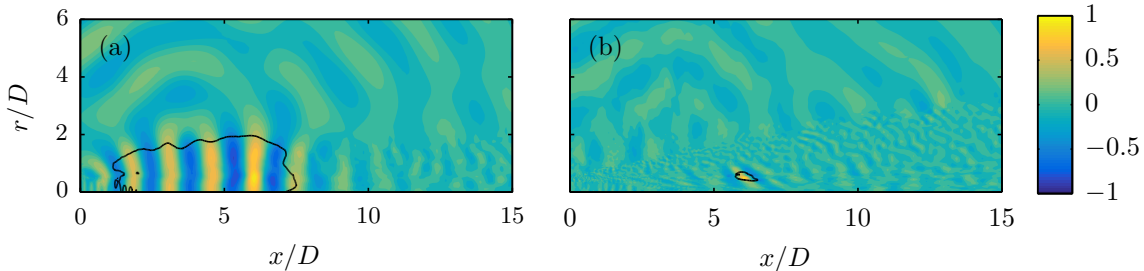


Figure 3: The real part of the complex coherence of (a) pressure and (b) streamwise-momentum forcing with respect to their reference values at $x_0/D = 6, r_0/D = 0.5$ for $St = 0.52$ and $m = 0$. The black lines bound the regions where the magnitude of the coherence is greater than 0.5.

IV.B. Coherence

The remaining off-diagonal terms in the CSD matrices are made up of correlations between every combination of variable and spatial coordinate. These are best described by the scaled quantity

$$\gamma_{\hat{u}\hat{v}}(\vec{x}_i, \vec{x}_j, m, \omega) = \frac{S_{\hat{u}\hat{v}}(\vec{x}_i, \vec{x}_j, m, \omega)}{\sqrt{S_{\hat{u}\hat{u}}(\vec{x}_i, \vec{x}_i, m, \omega)}\sqrt{S_{\hat{v}\hat{v}}(\vec{x}_j, \vec{x}_j, m, \omega)}}. \quad (19)$$

We call $\gamma_{\hat{u}\hat{v}}$ the (complex-valued) coherence, and the standard definition of coherence is given by its magnitude $|\gamma_{\hat{u}\hat{v}}|$. By construction, the coherence satisfies the condition $0 \leq |\gamma_{\hat{u}\hat{v}}| \leq 1$. Large and small values indicate a strong or weak relationship, respectively, between \hat{u} and \hat{v} .

The wavepackets within the jet cause extended regions of high coherence within the flow variables. For example, the contours in Figure 3(a) show the real part of the complex coherence of the pressure-field, relative to the pressure at the reference point $(x_0/D = 5, r_0/D = 0.5)$ for $St = 0.52$ and $m = 0$. The wavepacket structure is evident, and the region where the magnitude of the coherence is greater than one-half (demarcated by the solid line) extends more than six jet-diameters in the streamwise direction and two diameters in the radial direction. Figure 4 shows streamwise (top row) and radial (bottom row) slices of the coherence of the pressure-field relative to the pressure at three different reference points (columns) for $St = 0.17, 0.52$, and 0.86 and $m = 0$. The streamwise wavelength and decay-rate and the radial form of the wavepackets in the coherence-field depend strongly on frequency and the location of the reference point, as previously observed.³³ These variations can be attributed, at least in part, to the frequency and streamwise dependence of the Kelvin-Helmholtz modes whose growth and decay play a central role in the formation of wavepackets.

The properties of the coherence of the nonlinear forcing fields are quite different. The contours in Figure 3(b) show the real part of the complex coherence of the streamwise-momentum forcing, relative to its value at $(x_0/D = 5, r_0/D = 0.5)$ for $St = 0.52$ and $m = 0$. The streamwise and radial extent of the region where the coherence is larger than one-half is about an order-of-magnitude smaller than it was for the pressure. The coherent region is slightly inclined and elongated in the streamwise direction.

We next study the properties of the forcing coherence as a function of reference point and frequency. To limit the number of degrees of freedom, we focus on reference points along the jet lip-line $r/D = 0.5$. This choice is motivated by the high PSD of the forcing along the lip-line and also by the observation that the input modes for the leading resolvent modes have high support in this region, which implies that flow is sensitive to the forcing there. We have found that the coherence of the forcing field with respect to reference points with different r_0 -values is similar to those reported here as long as the reference point remains in regions of high PSD, as shown in Figure 2. Different coherence properties are found if the reference point is moved to regions with low PSD, but the coherence in these regions is probably irrelevant precisely because the PSD levels are low. We also focus on the axisymmetric mode ($m = 0$) of the streamwise momentum forcing, but note that similar trends hold for other forcing components and for the helical mode ($m = 1$). The forcing CSD matrices also contain inter-variable correlations. The magnitudes of the coherence of these terms were previously shown to be comparatively small,¹¹ so we do not consider them in the present investigation.

Figure 5 shows streamwise slices of the coherence of the streamwise-momentum forcing-field for $St = 0.17, 0.52$, and 0.86 relative to the reference points $x_0/D = 2, 6$, and 10 . These three points are prior to, near the

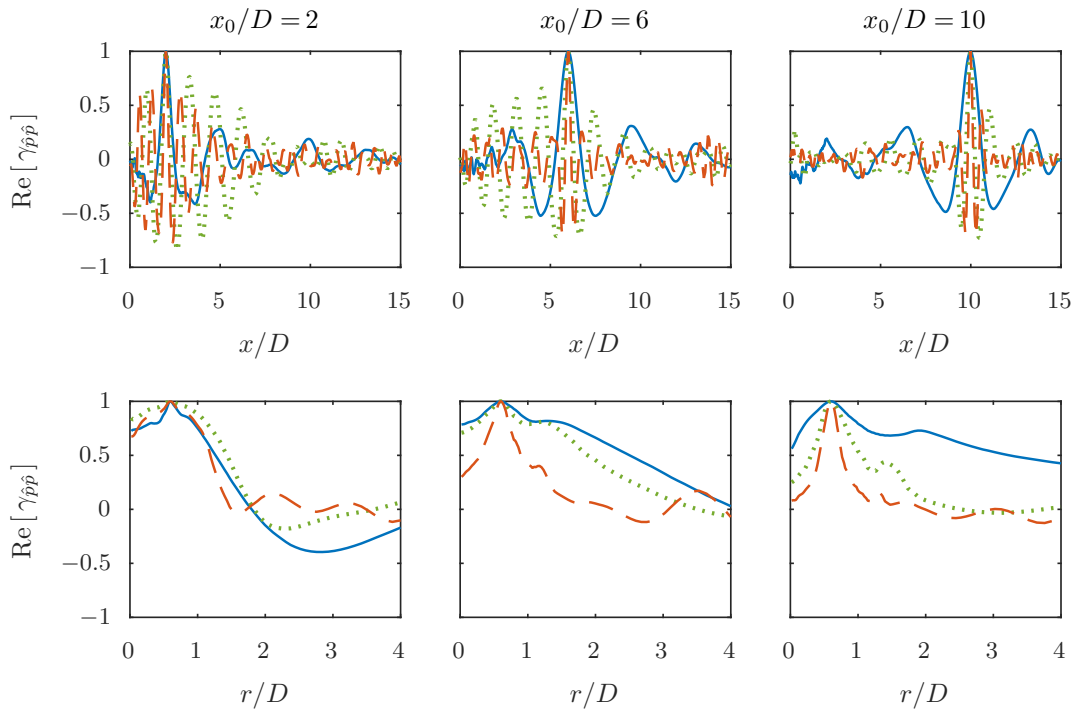


Figure 4: The real part of the complex-valued coherence of the pressure with respect to its reference values at $r_0/D = 0.5$ and $x_0/D = 2, 6,$ and 10 (left to right), plotted along the lines $r/D = 0.5$ (top row) and $x/D = x_0/D$ (bottom row) for $m = 0$ and: (—) $St = 0.17$; (---) $St = 0.52$; (- - -) $St = 0.86$.

end of, and past the end of the potential core, respectively. The horizontal axes in each column are centered at the respective reference point, but the streamwise extent is the same in each plot so that length-scales can be directly compared. From top to bottom, the rows show the magnitude and the real and imaginary parts of the coherence. Several properties are evident. First, the coherence magnitudes consist of peaks that are quite narrow compared to the coherence length-scales of the flow variables (compare the top rows of Figures 4 and 5, noting the different horizontal scales). The peaks are especially narrow for the reference point nearest the nozzle in the initial shear-layer and broadens as the reference point moves downstream. Notably, the shape and width of the peaks is essentially independent of frequency for all three reference points. On the other hand, the real and imaginary parts of the coherence show that each frequency has a different streamwise wavelength. However, this wavelength does not depend significantly on the reference point.

Figure 5 shows radial slices of the coherence of the streamwise-momentum forcing-field for the same three reference points and frequencies. Similar trends are observed. The peaks in the forcing magnitude are very narrow compared to the flow-field coherence profiles (compare the second row of Figure 4 to the first row of Figure 6). The peaks broaden as the reference point is moved downstream, and the widths are independent of frequency. The real and imaginary parts of the coherence show a wavelength that again depends primarily on the frequency and little on the location of the reference point.

In summary, the coherence fields of the nonlinear forcing terms consist of narrow peaks whose streamwise and radial widths depend on the location of the reference point (but not on frequency) and whose wavelengths depend on frequency (but not on location of the reference point).

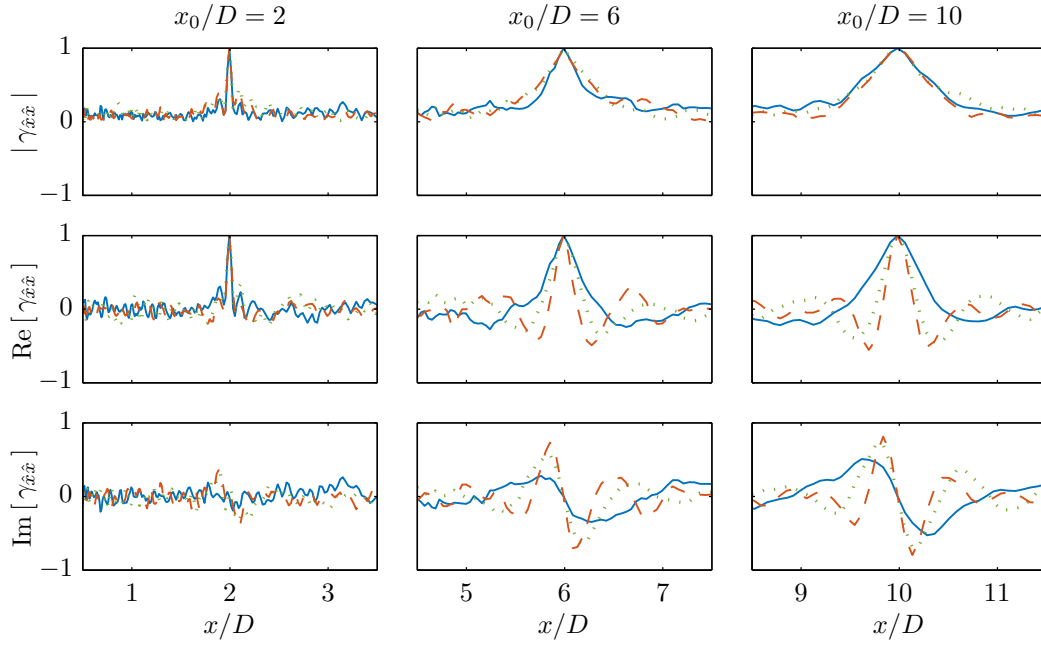


Figure 5: Streamwise profiles along the line $r/D = 0.5$ of the coherence of the streamwise-momentum forcing with respect to its reference values at $r_0/D = 0.5$ and $x_0/D = 2, 6,$ and 10 (left to right) for $m = 0$ and: (—) $St = 0.17$; (---) $St = 0.52$; (- - -) $St = 0.86$. From top to bottom, the rows show the magnitude, real part, and imaginary part of the coherence.

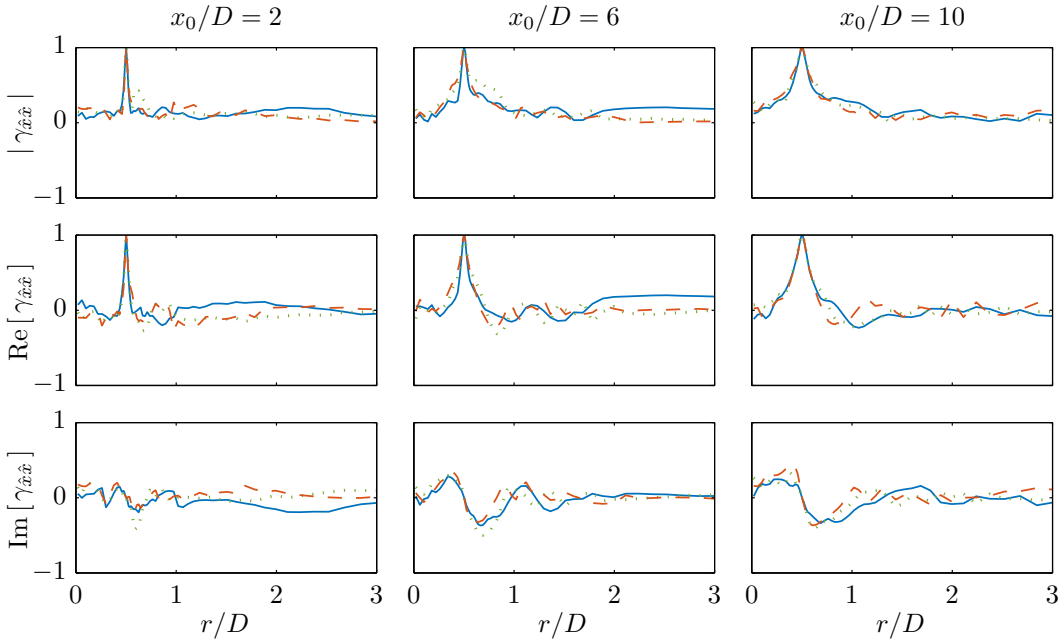


Figure 6: Radial profiles along the lines $x/D = x_0/D$ of the coherence of the streamwise-momentum forcing with respect to its reference values at $r_0/D = 0.5$ and $x_0/D = 2, 6,$ and 10 (left to right) for $m = 0$ and: (—) $St = 0.17$; (---) $St = 0.52$; (- - -) $St = 0.86$. From top to bottom, the rows show the magnitude, real part, and imaginary part of the coherence.

V. Modeling the forcing statistics

Next, we explore functions that could be used to approximate the forcing statistics in our resolvent-based statistical noise model. We compare the properties of the forcing statistics with a common fit-function used to represent similar source terms in acoustic analogy and stochastic jet-noise models and suggest a modified form that better captures the trends in the data. We also give some preliminary suggestions on how the parameters in the fit function might be predicted using quantities that could be obtained from a Reynolds-averaged Navier-Stokes (RANS) simulation.

V.A. Standard space-time fit functions

One of the most commonly used functions for approximating the two-point, two-time correlations of source terms in acoustic analogy and stochastic jet noise models is^{23,34-36}

$$R_{ff}(\vec{x}_0, \xi, \eta, \zeta, \tau) = R_0 \exp\left(-\frac{|\xi|}{\bar{u}_s \tau_s} - \frac{\ln 2}{l_s^2} ((\xi - \bar{u}_s \tau)^2 + \eta^2 + \zeta^2)\right), \quad (20)$$

where (ξ, η, ζ, τ) are displacements in (x, y, z, t) from the reference point \vec{x}_0 and $t_0 = 0$. The parameters l_r , τ_s , and \bar{u} are reference length, time, and convective velocity scales, respectively, and R_0 sets the amplitude of the correlations. All of these parameters are usually allowed to depend on the spatial reference point. The cross-spectral density tensor associated with this correlation function is obtained by taking the Fourier transform of equation (20) with respect to τ , giving

$$S_{\hat{f}\hat{f}}(\vec{x}_0, \xi, \eta, \zeta, \omega) = 2TR_0 \exp(-T^2\omega^2) \exp\left(-\frac{\ln 2}{l_s^2} (\eta^2 + \zeta^2)\right) \exp\left(-\frac{|\xi|}{\bar{u}_s \tau_s}\right) \exp\left(\frac{i\omega\xi}{\bar{u}_s}\right) \quad (21)$$

with $T = l_s / (2\sqrt{\ln 2} \bar{u}_s)$.

Some of the properties of this spectral-density function are consistent with the observations from the previous section. The streamwise amplitude of the coherence is determined by the third exponential term in equation (21). It is therefore independent of frequency but dependent on the location of the reference point since $\bar{u}_s \tau_s$ may depend on space. The radial distance from the reference point is equal to $\sqrt{\eta^2 + \zeta^2}$ so the radial amplitude of the coherence is determined by the second exponential term, which is also independent of frequency but dependent on the reference point since l_s may depend on space. The streamwise wavelength of the coherence is determined by the last exponential term and is therefore dependent on frequency.

There are also several discrepancies between equation (21) the observations from the previous section. The streamwise wavelength depends on the reference point since \bar{u}_s does. There is no radial wavelength at all. Most importantly, the first exponential term in equation (21) causes the power spectral density to decay with frequency as $\exp(-T^2\omega^2)$. This decay rate is roughly consistent with the decay rate of the energy of the *flow* variables, but the energy of the *forcing* terms was shown in Section IV to be independent of frequency up to at least $St = 1$.

There are several other fit function that have been suggested in the literature that are in principle capable of producing PSDs that are independent of frequency, at least for low frequencies.³⁷⁻³⁹ However, the frequency-dependence of this class of functions is described by the scaled variable $\tilde{\omega} = \omega l_s / \bar{u}_s$. Since l_s and \bar{u}_s depend on the reference point, frequency and spatial effects are not decoupled, in contrast to the results of our analysis. Despite this issue, more work is required to fairly assess the overall properties of the spectral fits achievable with these fit functions.

V.B. A simple spectral fit function

Inspired by our observations in Section IV, we propose an alternative, simple fit function for the cross-spectral density:

$$S_{\hat{f}\hat{f}}(\vec{x}_0, \xi, \rho, \omega) = S_0 \exp\left(-\frac{|\xi|}{l_x}\right) \exp(ik_x \xi) \exp\left(-\frac{|\rho|}{l_r}\right) \exp(ik_r \rho), \quad (22)$$

where ρ is the radial distance from the reference point, $l_x = l_x(x_0)$, $l_r = l_r(r_0)$, $k_x = k_x(\omega)$, $k_r = k_r(\omega)$, and $S_0 = S_0(x_0, r_0)$. This function respects all of the properties of the forcing PSD and coherence discussed in the previous section. Moreover, its simple form is useful for further exploring and quantifying the properties of the forcing coherence.

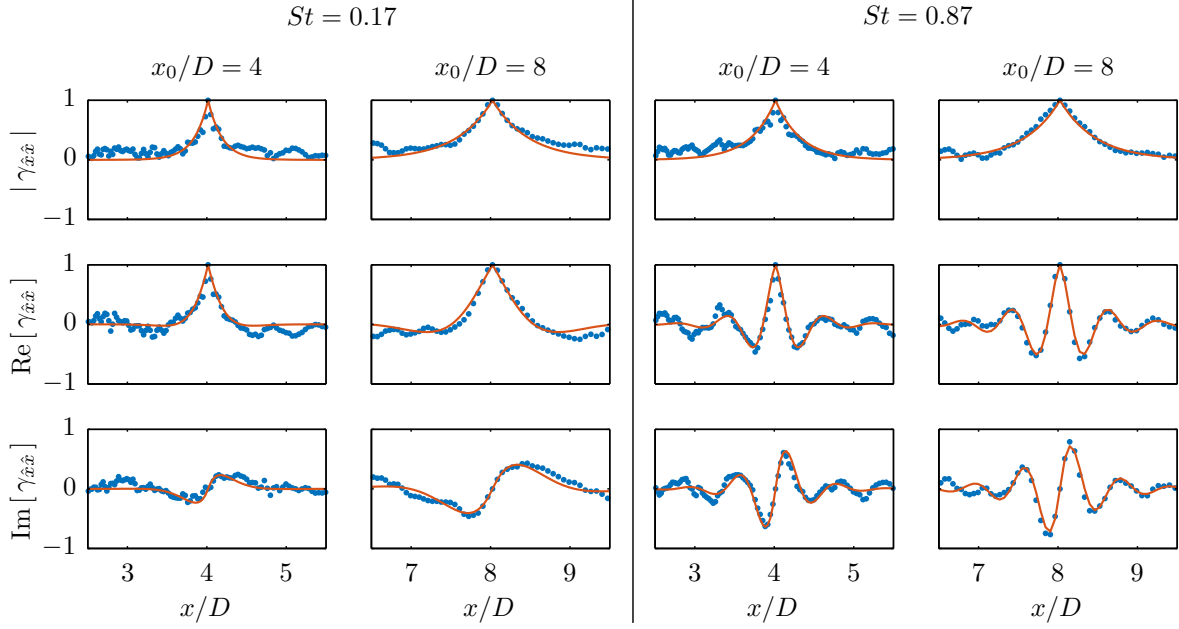


Figure 7: Comparison between LES values (\bullet) and the fit function (---) for streamwise profiles of the coherence of the streamwise momentum forcing with respect to its reference values at $x_0/D = 4$ and 8 and $r_0/D = 0.5$ for $St = 0.17$ and 0.87 and $m = 0$, plotted along the line $r/D = 0.5$. From top to bottom, the rows show the magnitude, real part, and imaginary part of the coherence.

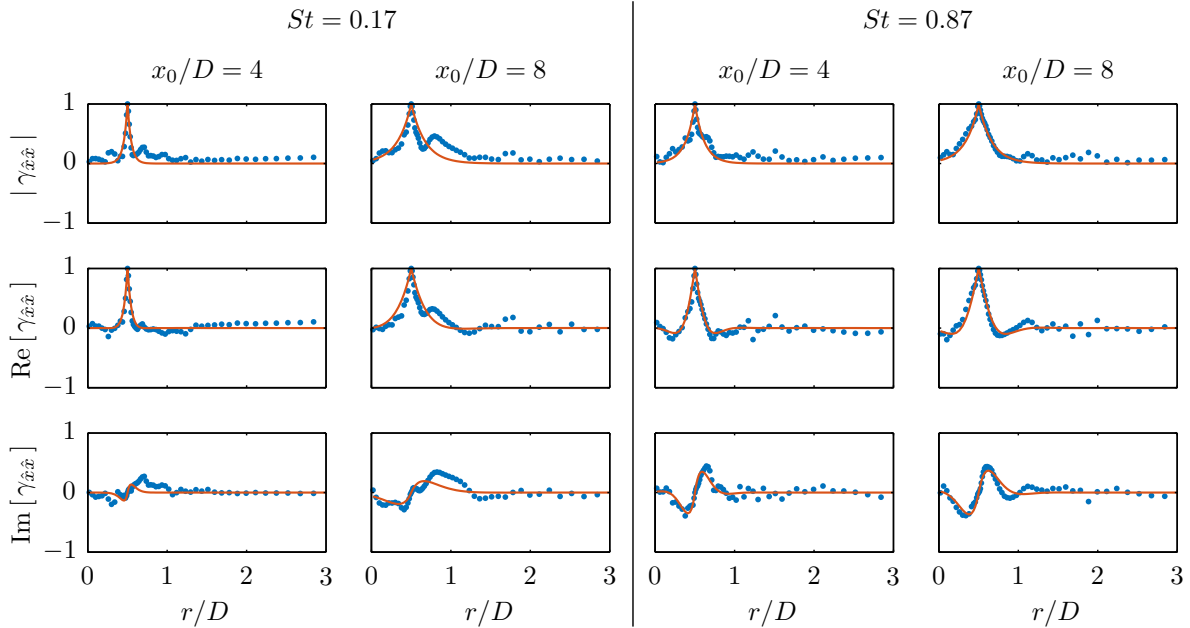


Figure 8: Comparison between LES values (\bullet) and the fit function (---) for radial profiles of the coherence of the streamwise momentum forcing with respect to its reference values at $x_0/D = 4$ and 8 and $r_0/D = 0.5$ for $St = 0.17$ and 0.87 and $m = 0$, plotted along the lines $x/D = x_0/D$. From top to bottom, the rows show the magnitude, real part, and imaginary part of the coherence.

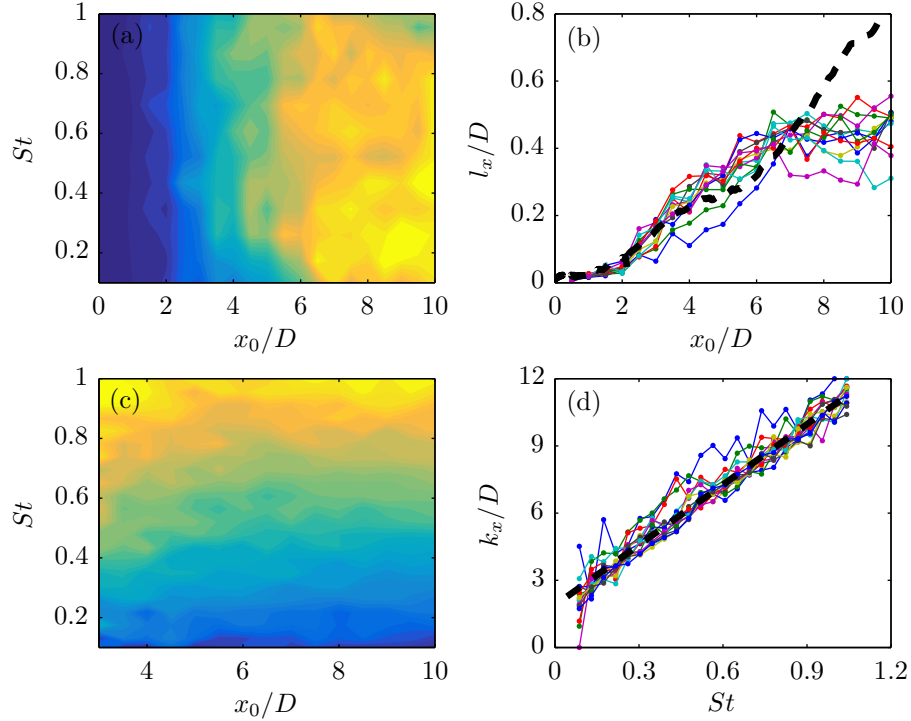


Figure 9: Optimal fit parameters: (a) contours of l_x/D as a function of x_0/D and St ; (b) line-plots of l_x/D as a function of x_0/D for various values of St ; (c) contours of k_x/D as a function of x_0/D and St ; (d) line-plots of k_x/D as a function of St for various values of x_0/D . In both contour plots, the contour levels are evenly distributed between minimum and maximum values of the plotted quantity.

With this in mind, we assess the quality of the fits that can be obtained using this function. Since it is separable in ξ and ρ , the parameter pairs (l_x, k_x) and (l_r, k_r) are decoupled and can be determined by fitting the one-dimensional streamwise and radial coherence profiles, respectively, that were discussed in Section IV. This is accomplished using a nonlinear least-squares algorithm. Rather than forcing the ξ , ρ , and ω dependencies noted above, we allow the least-squares algorithm to choose the best value for each reference point and frequency and assess *a posteriori* whether the optimal fits do indeed exhibit the expected dependencies.

Figure 7 compares streamwise slices of the LES coherence data with the fits provided by equation (22) with optimal l_x and k_x values for two reference points and two frequencies. In all cases, the function provides an excellent fit. In particular, the sharp peak produced by the $\exp(-|\xi|/l_x)$ form matches the data well; fits of the form $\exp(-\xi^2/l_x^2)$ produce inferior results. Figure 8 compares radial slices of the coherence data with the fits provided by equation (22) with optimal l_r and k_r values for the same two reference points and frequencies. The quality of the fits is again quite good, although the radial coherence profiles tend to be slightly skewed, which cannot be captured by the symmetric fit function. Again, the sharp peaks provided by the absolute value term matches the data better than a Gaussian form such as the one in equation 21.

Figure 9 shows the optimal streamwise length scale l_x and wavenumber k_x as a function of the streamwise reference point location and frequency. Similar plots can be generated for the radial fit parameters but are omitted for brevity. The l_x values are shown in two different ways in the top row. Figure 9(a) shows contours of l_x as a function of x_0/D and St ; the contours are evenly distributed between the minimum and maximum values. While there is some noise in the results as a result of noise in the data due to finite levels of convergence, it is clear that l_x varies primarily with x_0 . Figure 9(b) shows line plots of l_x/D for all St values as a function of X_0/D . A reasonably good collapse is observed. The back dashed line will be discussed later. The bottom row of Figure 9 shows the optimal k_x values in a similar manner. Figure 9(c) shows contours of k_x as a function of x_0/D and St , with levels evenly distributed between the minimum and maximum value.

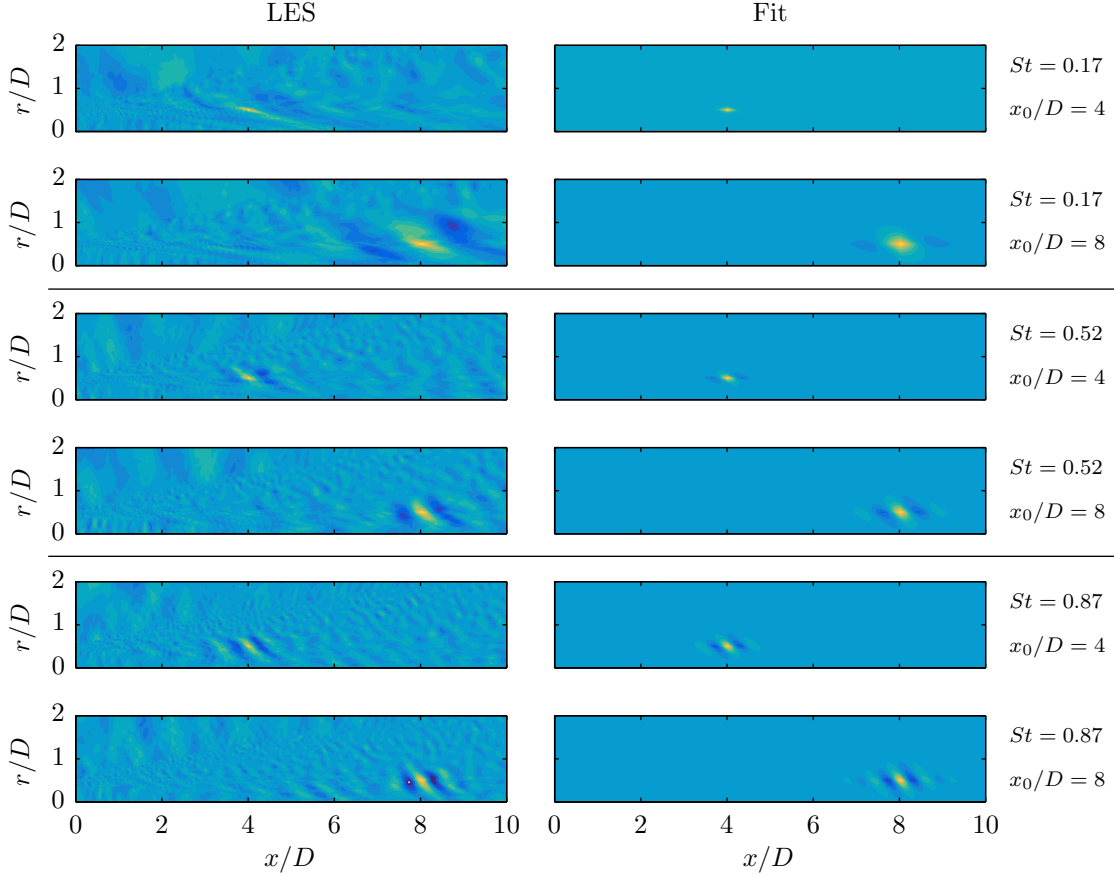


Figure 10: The real part of the LES (left) and fit (right) coherence of the streamwise-momentum forcing with respect to its reference values at $x_0/D = 4$ and 8 and $r_0/D = 0.5$ for $m = 0$ and $St = 0.17, 0.52$, and 0.86 .

This time, the variation is primarily in the St -direction. Accordingly, k_x/D values are plotted in Figure 9(d) as a function of St for all values of reference point locations. The collapse of the curves for different reference points is quite good. Furthermore, it is clear that the wavenumber depends *linearly* on the frequency, but with a non-zero intercept.

The two-dimensional coherence fields are recovered from the one-dimensional fits using equation (22). The real part of the coherence is shown in Figure 10 for two reference points and three frequencies. The fits capture the essential features in all cases and are especially good for the higher two frequencies. The fits successfully reproduce the inclination of the coherence contours observed in the data. One discrepancy is that the axes along which the coherence fields decay also appear to be slightly tilted in a counter-clockwise direction. This cannot be captured by the separable fit function, but could be incorporated using a fit function written in terms of rotated coordinates.

V.C. RANS modeling

Our results so far have identified clear trends in the forcing statistics as well as a simple fit-function that mimics these properties with reasonable accuracy. However, to make the overall noise-model predictive, it would be necessary to quantitatively predict the functions $l_x(x_0)$, $l_r(r_0)$, $k_x(\omega)$, $k_r(\omega)$, and $S_0(x_0, r_0)$ without recourse to tuning parameters. Acoustic analogy source models attempt to achieve this using quantities that can be extracted from a Reynolds-averaged Navier-Stokes (RANS) simulation, and a similar strategy could be pursued for our model. We have found that the forcing PSD $S_0(x_0, r_0)$ is nicely approximated by the squared turbulent kinetic energy, which is plotted in Figure 11 using the same logarithmic scale used in Figure 2.

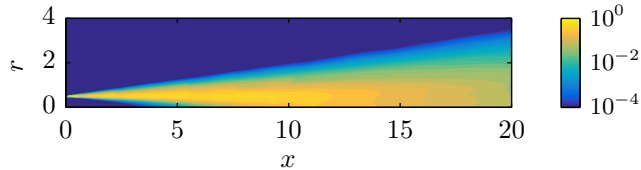


Figure 11: Squared turbulent kinetic energy computed from the LES data, scaled by its maximum value and plotted using the same logarithmic scale used in Figure 2. This provides an excellent approximation of the forcing PSD.

Additionally, spatially-dependent length scales obtained from basic RANS turbulence models could be used to model the functions $l_x(x_0)$ and $l_r(r_0)$. For example, the black dashed line in Figure 9(b) is proportional to the length scale $l = k^{3/2}/\epsilon$, where k is the turbulent kinetic energy and ϵ is the turbulent dissipation rate. Finally, the functions $k_x(\omega)$ and $k_r(\omega)$ could be related to convective velocities. For example, the black dashed line in Figure 9(d) shows the function $k_x/D = 2\pi(St/0.7 + 0.3)$, which provides a good fit for $k_x(\omega)$. The value 0.7 is a common approximation of the convective velocity of large-scale structures, as a fraction of the jet velocity. We currently have no intuitive explanation for the constant value 0.3. Nevertheless, this sort of approach will inevitably require a number of scaling parameters which are unlikely to be universal over a wide range of operating conditions. A alternative approach that might avoid this issue would be to design an operator-based filter that generates the desired forcing statistics, as discussed by Zare *et al.*⁴⁰

VI. Statistics of the nonlinear forcing terms in a low-Reynolds-number jet

Finally, we show that for the low-Reynolds-number jet the forcing fields are quite different than those observed so far for the high-Reynolds-number case. Figure 12 is analogous to Figure 1, showing the total energy of each flow-field and forcing-field variable as a function of frequency. The flow field again shows an overall decay with increasing frequency apart from the strong peaks associated with trapped acoustic modes. However, unlike the high-Reynolds number jet, the forcing energy is also dependent on frequency for the low-Reynolds-number jet. Furthermore, the coherence length-scales of the flow and forcing fields are of the same order in the low-Reynolds-number jet. This is clearly evident in Figure 13, which shows streamwise profiles of the real part of the pressure and axial momentum coherence fields for the low-Reynolds-number jet for three frequencies and reference points. Additionally, the magnitude of the forcing coherence for the low-Reynolds-number jet clearly depends on frequency. These observations stand in stark contrast to the results for the high-Reynolds-number jet.

The similarity between the flow and forcing coherence fields in the low-Reynolds-number jet is likely indicative of direct nonlinear interaction between wavepackets. Nonlinear wavepacket interactions are at the center of several nonlinear jet-noise models. Several authors^{41–43} have used the nonlinear parabolized stability equations, which in an approximate sense account for nonlinear interactions between the dominant weakly nonparallel instability modes at a discrete set of frequencies and azimuthal wavenumbers. Other models focus specifically on low-frequency difference modes resulting from the nonlinear interaction between two instability waves with similar frequencies^{44,45} or nonlinear interaction between a pair of helical instability modes with nearly the same frequencies but opposite azimuthal wavenumbers.⁴⁶ While these sorts of nonlinear interactions have been shown to increase acoustic radiation in low-Reynolds-number transitional jets, the relevance of these mechanisms in realistic high-Reynolds-number turbulent jets has not been established. Nonlinear products of two wavepacket structures with extended regions of coherence should itself have an extended region of coherence. This is observed in the coherence fields of the nonlinear forcing terms at low Reynolds number but not at high Reynolds number, suggesting that these nonlinear wavepacket interaction occur at low Reynolds numbers but are likely absent at high Reynolds numbers.

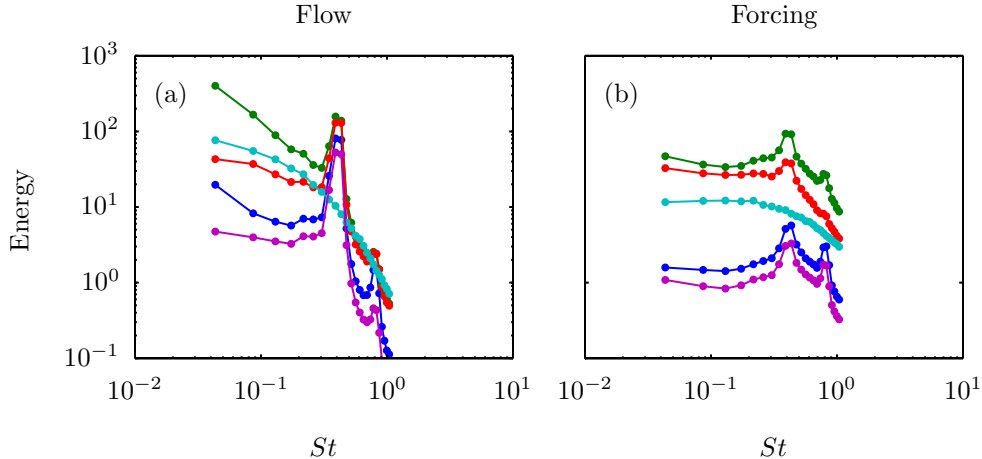


Figure 12: Total energy, defined as the spatially-integrated power spectral density, for each flow (left) and forcing (right) variable in the low-Reynolds-number jet as a function of frequency for $m = 0$. The flow variables are, from top to bottom, streamwise, radial, and azimuthal velocity, specific density, and pressure. The forcing terms act on the axial, radial, and azimuthal momentum equations, the continuity equation, and the energy equation.

VII. Summary and conclusions

This paper continues the development of the resolvent-based model proposed by Towne *et al*¹¹ designed to capture the full second-order statistics of the jet. The model requires an approximation of the cross-spectral density tensor of nonlinear forcing terms, and the focus of this paper was to highlight the properties of these statistics using LES data. For a high-Reynolds-number jet, we found that the power-spectral densities of the forcing do not depend on frequency within the range $0.04 < St < 1.04$ for $m = 0$ and 1. The coherence fields of the forcing consist of peaks that are spatially compact compared to the coherence length-scales of the flow variables. The widths of these peaks increase as the coherence reference point is moved downstream but are independent of frequency. On the other hand, the streamwise and radial wavelengths of the coherence fields increase with frequency but are independent of the location of the reference point.

Some of these properties are not captured by a function used by numerous authors to fit source correlations within the context of acoustic analogy of stochastic models. We propose a modified fit function directly in the frequency domain that does respect the observed properties of the spectral densities and show that it leads to good approximations of the observed forcing coherence fields. Then, we discuss how RANS quantities might be used to predict some of the fit parameters. We show that the squared turbulent kinetic energy provides an excellent approximation of the frequency-independent forcing PSD. Similarly, standard turbulent length-scales that can be obtained from RANS provide a reasonable estimate of some of the coherence length-scales. Still, there is much more work to be done if the model is to be made entirely predictive.

Lastly, we briefly examined the forcing statistics in a low-Reynolds-number jet and found significant differences. The forcing PSD is not frequency-independent and the coherence length scales of the forcing are of the same order as those of the flow-field. These findings may indicate the presence of direct nonlinear wavepacket interactions in the low-Reynolds-number jet that are absent in the high-Reynolds-number case. This suggests that nonlinear models may be more appropriate at low Reynolds numbers.

Acknowledgments

The LES study was supported by NAVAIR SBIR project, under the supervision of Dr. John T. Spyropoulos. The main LES calculations were carried out on CRAY XE6 machines at DoD HPC facilities in ERDC DSRC. A.T. was supported by a postdoctoral fellowship funded by NASA.

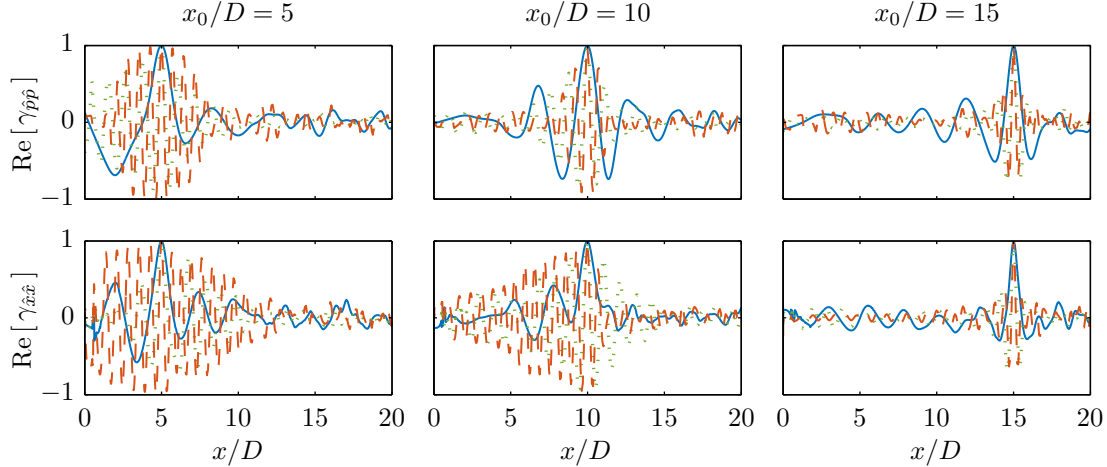


Figure 13: Streamwise profiles of the real part of the coherence of the pressure (top) and streamwise-momentum forcing (bottom) with respect to their reference values at $r_0/D = 0.5$ and $x_0/D = 5, 10,$ and $15,$ plotted along the line $r/D = 0.5$ for $m = 0$ and: (—) $St = 0.17;$ (- - -) $St = 0.52;$ (- - -) $St = 0.86.$

References

- ¹Jordan, P. and Colonius, T., “Wave Packets and Turbulent Jet Noise,” *Annu. Rev. Fluid Mech.*, Vol. 45, 2013, pp. 173–195.
- ²Gudmundsson, K. and Colonius, T., “Instability wave models for the near-field fluctuations of turbulent jets,” *J. Fluid Mech.*, Vol. 689, 2011, pp. 97–128.
- ³Sinha, A., Rodríguez, D., Brès, G. A., and Colonius, T., “Wavepacket models for supersonic jet noise,” *J. Fluid Mech.*, Vol. 742, 2014, pp. 71–95.
- ⁴Schmidt, O. T., Towne, A., Colonius, T., Jordan, P., Jaunet, V., Cavalieri, A. V. G., and Brès, G. A., “Super- and multi-directional acoustic radiation by linear global modes of a turbulent jet,” *AIAA Paper #2016-2808*, 2016.
- ⁵Baqui, Y. B., Agarwal, A., Cavalieri, A., and Sinayoko, S., “Nonlinear and linear noise source mechanisms in subsonic jets,” *AIAA Paper #2013-2279*, 2013.
- ⁶Jordan, P., Colonius, T., Brès, G. A., Zhang, M., Towne, A., and Lele, S., “Modeling intermittent wavepackets and their radiated sound in a turbulent jet,” Tech. rep., Proceedings of the Center for Turbulence Research summer program, 2014.
- ⁷Cavalieri, A. V. G., Jordan, P., Agarwal, A., and Gervais, Y., “Jittering wave-packet models for subsonic jet noise,” *J. Sound Vib.*, Vol. 330, No. 18, 2011, pp. 4474–4492.
- ⁸Freund, J. and Colonius, T., “Turbulence and sound-field POD analysis of a turbulent jet,” *Int. J. Aeroacoust.*, Vol. 8, No. 4, 2009, pp. 337–354.
- ⁹Towne, A., Colonius, T., Jordan, P., Cavalieri, A. V. G., and Brès, G. A., “Stochastic and nonlinear forcing of wavepackets in a Mach 0.9 jet,” *AIAA Paper #2015-2217*, 2015.
- ¹⁰Cavalieri, A. V. G. and Agarwal, A., “Coherence decay and its impact on sound radiation by wavepackets,” *J. Fluid Mech.*, Vol. 748, 2014, pp. 399–415.
- ¹¹Towne, A., Brès, G. A., and Lele, S. K., “Toward a resolvent-based statistical jet-noise model,” *Annual Research Briefs*, Center for Turbulence Research, Stanford University, 2016.
- ¹²Schmid, P. J. and Henningson, D. S., *Stability and Transition in Shear Flows*, Vol. 142, Springer Science & Business Media, 2001.
- ¹³Jovanovic, M. R. and Bamieh, B., “Componentwise energy amplification in channel flows,” *J. Fluid Mech.*, Vol. 534, 2005, pp. 145–183.
- ¹⁴McKeon, B. and Sharma, A., “A critical-layer framework for turbulent pipe flow,” *J. Fluid Mech.*, Vol. 658, 2010, pp. 336–382.
- ¹⁵Garnaud, X., Lesshafft, L., Schmid, P., and Huerre, P., “The preferred mode of incompressible jets: linear frequency response analysis,” *J. Fluid Mech.*, Vol. 716, 2013, pp. 189–202.
- ¹⁶Jeun, J., Nichols, J. W., and Jovanović, M. R., “Input-output analysis of high-speed axisymmetric isothermal jet noise,” *Phys. Fluids*, Vol. 28, No. 4, 2016.
- ¹⁷Semeraro, O., Jaunet, V., Jordan, P., Cavalieri, A. V. G., and Lesshafft, L., “Stochastic and harmonic optimal forcing in subsonic jets,” *AIAA Paper #2016-2935*, 2016.
- ¹⁸Towne, A., *Advancements in jet turbulence and noise modeling: accurate one-way solutions and empirical evaluation of the nonlinear forcing of wavepackets*, Ph.D. thesis, California Institute of Technology, 2016.
- ¹⁹Bechara, W., Bailly, C., Lafon, P., and Candel, S. M., “Stochastic approach to noise modeling for free turbulent flows,” *AIAA J.*, Vol. 32, No. 3, 1994.

- ²⁰Billson, M., Eriksson, L.-E., and Davidson, L., “Jet noise modeling using synthetic anisotropic turbulence,” *AIAA Paper #2004-3028*, 2004.
- ²¹Lafitte, A., Laurendeau, E., La Garrec, T., and Bailly, C., “A study based on the sweeping hypothesis to generate stochastic turbulence,” *AIAA Paper #2011-2888*, 2011.
- ²²Siefert, M. and Ewert, R., “Sweeping sound generation in jets realized with a random particle-mesh method,” *AIAA Paper #2009-3369*, 2009.
- ²³Tam, C. K. W. and Auriault, L., “Jet mixing noise from fine-scale turbulence,” *AIAA J.*, Vol. 37, No. 2, 1999, pp. 145–153.
- ²⁴Goldstein, M., “A generalized acoustic analogy,” *J. Fluid Mech.*, Vol. 488, 2003, pp. 315–333.
- ²⁵Brès, G. A., Ham, F. E., Nichols, J. W., and Lele, S. K., “Unstructured Large-Eddy Simulations of Supersonic Jets,” *AIAA J.*, 2017.
- ²⁶Brès, G. A., Jaunet, J., Le Rallic, M., Jordan, P., Colonius, T., and Lele, S. K., “Large eddy simulation for jet noise: the importance of getting the boundary layer right,” *AIAA Paper #2015-2535*, 2015.
- ²⁷Brès, G. A., Jaunet, V., Le Rallic, M., Jordan, P., Towne, A., Schmidt, O., Colonius, T., Cavalieri, A. V. G., and Lele, S. K., “Large eddy simulation for jet noise: azimuthal decomposition and intermittency of the radiated sound,” *AIAA Paper #2016-3050*, 2016.
- ²⁸Freund, J. B., “Noise sources in a low-Reynolds-number turbulent jet at Mach 0.9,” *J. Fluid Mech.*, Vol. 438, 2001, pp. 277–305.
- ²⁹Towne, A., Cavalieri, A. V. G., Jordan, P., Colonius, T., Jaunet, V., Schmidt, O. T., and Brès, G. A., “Trapped acoustic waves in the potential core of subsonic jets,” *AIAA Paper #2016-2809*, 2016.
- ³⁰Towne, A., Cavalieri, A. V. G., Jordan, P., Colonius, T., Schmidt, O. T., Jaunet, V., and Brès, G. A., “Acoustic resonance in the potential core of subsonic jets,” *submitted*.
- ³¹Schmidt, O. T., Towne, A., Colonius, T., Cavalieri, A. V. G., Jordan, P., and Brès, G. A., “Wavepackets and trapped acoustic modes in a turbulent jet: coherent structure eduction and global stability,” *submitted*.
- ³²Schmidt, O. T., Colonius, T., and Brès, G. A., “Linear dynamics of large-scale structures in turbulent jets,” *Tenth International Symposium on Turbulence and Shear Flow Phenomena*, 2017.
- ³³Jaunet, V., Jordan, P., and Cavalieri, A. V. G., “Two-point coherence of wavepackets in turbulent jets,” *AIAA Paper #2016-3058*, 2016.
- ³⁴Ffowcs-Williams, J. E., “The Noise from Turbulence Convected at High Speed,” *Phil. Trans. R. Soc. A.*, Vol. 255, No. 1061, 1963, pp. 469–503.
- ³⁵Morris, P. J. and Farassat, F., “Acoustic analogy and alternative theories for jet noise prediction,” *AIAA J.*, Vol. 40, No. 4, 2002, pp. 671–680.
- ³⁶Karabasov, S., Afsar, M., Hynes, T., Dowling, A., McMullan, W., Pokora, C., Page, G., and McGuirk, J., “Jet noise: acoustic analogy informed by large eddy simulation,” *AIAA J.*, Vol. 48, 2010, pp. 1312–1325.
- ³⁷Harper-Bourne, M., “Jet noise turbulence measurements,” *AIAA Paper #2003-3214*, 2003.
- ³⁸Leib, S. and Goldstein, M., “Hybrid source model for predicting high-speed jet noise,” *AIAA J.*, Vol. 49, No. 7, 2011, pp. 1324–1335.
- ³⁹Afsar, M. Z., Sescu, A., and Leib, S. J., “Predictive capability of low frequency jet noise using an asymptotic theory for the adjoint vector Green’s function in non-parallel flow,” *AIAA Paper #2016-2804*, 2016.
- ⁴⁰Zare, A., Jovanović, M. R., and Georgiou, T. T., “Colour of turbulence,” *J. Fluid Mech.*, Vol. 812, 2017, pp. 636–680.
- ⁴¹Malik, M. and Chang, C.-L., “Nonparallel and nonlinear stability of supersonic jet flow,” *Comput. Fluids*, Vol. 29, No. 3, 2000, pp. 327–365.
- ⁴²Cheung, L. and Lele, S., “Aeroacoustic noise prediction and the dynamics of shear layers and jets using the nonlinear parabolized stability equations,” Tech. Rep. TF-103, 2007.
- ⁴³Itasse, M., Brazier, J.-P., Léon, O., and Casalis, G., “Parabolized Stability Equations analysis of nonlinear interactions with forced eigenmodes to control subsonic jet instabilities,” *Phys. Fluids*, Vol. 27, No. 8, 2015.
- ⁴⁴Sandham, N. D., Morfey, C., and Hu, Z., “Nonlinear mechanisms of sound generation in a perturbed parallel jet flow,” *J. Fluid Mech.*, Vol. 565, 2006, pp. 1–23.
- ⁴⁵Suponitsky, V., Sandham, N. D., and Morfey, C. L., “Linear and nonlinear mechanisms of sound radiation by instability waves in subsonic jets,” *J. Fluid Mech.*, Vol. 658, 2010, pp. 509–538.
- ⁴⁶Wu, X. and Huerre, P., “Low-frequency sound radiated by a nonlinearly modulated wavepacket of helical modes on a subsonic circular jet,” *J. Fluid Mech.*, Vol. 637, 2009, pp. 173–211.